Transforming understanding of paleomagnetic recording in igneous rocks: Insights from aging experiments on lava samples and the causes and consequences of 'fragile' curvature in Arai plots

L. Tauxe[1*], C.N. Santos[1], B. Cych[1], X. Zhao[2], A.P. Roberts[2]

[1]Scripps Institution of Oceanography, University of California, San Diego, La Jolla, CA, USA
[2]Research School of Earth Sciences, Australian National University, Canberra, Australia

Key Points:

- Unequal blocking/unblocking temperature spectra can lead to biased paleointensity estimates.
- Inequality grows through time in samples with coarser magnetic grain sizes.
- Quantifying curvature in Arai plots and the use of iFORCs can identify possibly biased results.

[*]National Science Foundation

Corresponding author: Lisa Tauxe, ltauxe@ucsd.edu

Abstract

The theory for recording of thermally blocked remanences predicts a quasi-linear relationship between low fields like the Earth's in which rocks cool and acquire a magnetization. This serves as the foundation for estimating ancient magnetic field strengths. Addressing long-standing questions concerning Earth's magnetic field require a global paleointensity dataset, but recovering the ancient field strength is complicated because the theory only pertains to uniformly magnetized particles. A key requirement of a paleointensity experiment is that a magnetization blocked at a given temperature should be unblocked by zero-field reheating to the same temperature. However, failure of this requirement occurs frequently and the causes and consequences of failure are poorly understood. Recent experiments demonstrate that the remanence in many samples typical of those used in paleointensity experiments is unstable, and exhibits an "aging" effect in which the unblocking temperature spectrum changes over only a few years resulting in non-ideal experimental behavior. While a fresh remanenence may conform to the requirement of equality of blocking and unblocking temperatures, aged remanences may not. Blocking temperature spectra can be unstable (fragile), which precludes reproduction of the conditions under which the original magnetization was acquired. This limits our ability to acquire accurate and precise ancient magnetic field strength estimates because differences between known and estimated fields can be significant (up to 10 μT) for individual specimens, with a low field bias. Fragility of unblocking temperature spectra appears to be related to grain size and may be related to features observed in first-order reversal curves.

Plain Language Summary

Earth's magnetic field acts as a shield against energetic solar storms and is thought to have been important in the evolution of life on Earth. The magnetic field is currently reducing in strength. Answering questions such as 'What is the average field?' and 'What is the likelihood of a collapse associated with a reversal or excursion?' depends on our understanding of past field behavior. There are no human measurements of field strength prior to the 19^{th} century, so we rely on geological and archaeological records. A great deal of effort has been put into experimental protocols to develop reliable records of field strength and to assess data reliability. Yet, mysteries remain regarding the nature of these so-called 'paleomagnetic' records. This paper focuses on expanding our understanding of magnetic recording in lava samples, which are one of the main archives used in paleointensity studies. In particular, we investigate the causes and consequences of failure of the principal assumptions in paleointensity experiments.

1 Introduction

The strength of the geomagnetic field has been a focus of geophysical research since the 1930s, starting with the work of Koenigsberger (1936) and Thellier (1938) and continuing today (see review of Tauxe and Yamazaki (2015)). Absolute paleointensity experiments rely on the assumption from Néel theory (Néel, 1955) that thermal remanent magnetizations (TRMs) are related quasi-linearly to the field in which a sample cooled and are generally based on normalization of remanences in controlled laboratory fields.

Despite decades of effort, fundamental problems remain with the methods used to extract reliable records of field strength. Paleointensity experiments involve a variety of protocols and there is no consensus on what materials might be suitable for the experiment or what constitutes a 'reliable' result. Although the paleointensity community recognized early the value of testing methods on materials with TRMs acquired in known fields (e.g., Abokodair, 1977; Tanaka & Kono, 1991), recent compilations suggest that even a single lava flow can give widely divergent results (Cromwell et al., 2015; Tauxe et al., 2016; Cai et al., 2017) with different methods yielding significantly different results (Cromwell et al., 2018).

Most paleointensity data in global paleomagnetic databases, e.g., the MagIC database (Tauxe et al., 2016) or the PINT database (Biggin, 2010), were obtained through some variant of the classic Koenigsberger-Thellier-Thellier (KTT) double heating technique (Koenigsberger, 1938; Thellier & Thellier, 1959) where the initial remanence (assumed to be a TRM) is replaced in a step-wise fashion with a laboratory acquired partial TRM (pTRM). The basic theoretical underpinning of these experiments are the so-called 'Thellier laws' (e.g., Thellier & Thellier, 1959) that concern pTRMs (the remanence acquired by cooling through two temperatures T_1, T_2 below the Curie Temperature). These are: 1) the Law of Reciprocity, where the blocking temperature (T_b) at which a pTRM was acquired is the same at which it is destroyed (the unblocking temperature, T_{ub}), 2) the Law of Independence, where pTRMs blocked between two temperature steps are independent of pTRMs acquired at different blocking temperatures, and 3) the Law of Additivity, where the total TRM (TTRM) is the sum of all pTRMs.

Many experimental protocols specify the order in which steps are performed. The one we use here is the so-called IZZI protocol (Yu et al., 2004; Tauxe & Staudigel, 2004). In this approach, specimens are heated to a given temperature and then cooled either in the presence of a controlled laboratory field (an in-field step) or in zero field (a zero-field step). The order (in-field followed by a zero-field step, IZ) alternates with a zero-field step first followed by an in-field step (ZI).

Despite widespread use, KTT techniques (including the IZZI method) have drawbacks in practice. These include complications such as changing of the ability to acquire a pTRM through chemical alteration during the double heating experiments (Coe, 1967), non-linearity of the TRM with applied field (Selkin et al., 2007), and anisotropy of the remanence tensor (Aitken et al., 1981). These phenomena can in many cases be detected, and in the latter two cases corrected for. However, there are more difficult complications with less well understood causes and consequences. For example, there is increasing evidence that paleointensity estimates from materials with non-linear Arai plots are biased (Krása et al., 2003; Shaar & Tauxe, 2015; Cromwell et al., 2015; Smirnov et al., 2017; Cromwell et al., 2018). However, the causes of possible bias are poorly understood and appropriate remedies are, therefore, unavailable. We suspect that the most likely cause of bias is failure of the Law of Reciprocity.

The Law of Reciprocity requires that a pTRM acquired by cooling through a particular temperature, T_b, can be removed (unblocked) by heating to the same temperature (T_{ub}) and cooling in zero field. As a conceptual model to illustrate the role of similar or different blocking and unblocking temperature spectra, we use a phenomenological approach similar to that taken by Paterson et al. (2015) (see also Fabian (2001); Yu et al. (2004), and Biggin (2006)). We draw synthetic (un)blocking temperature spectra from a scaled beta distribution with shape parameters (α and β). When Thellier's laws are obeyed, particularly the Law of Reciprocity, blocking and unblocking temperature spectra are identical (Figure 1a). When subjected to a KTT type experiment, the initial TRM is replaced by pTRMs in a step-wise fashion (Figure 1b). In the ideal case, there is a linear relationship between the TRM remaining after heating to a given temperature step and the pTRM gained as shown in the Arai plot in Figure 1c.

An IZZI experiment for the hypothetical case shown in Figure 1d-f, where the mean of the blocking temperature spectrum was 400°C and the mean of the unblocking temperature spectrum was 350°C, is shown in Figure 2. The IZZI experiment consists of a series of demagnetization (zero-field heating steps) and remagnetization (in-field heating steps) steps. The order in which the demagnetization/remagnetization steps are performed alternates between zero-field first followed by in-field (ZI) and in-field first followed by zero-field (IZ) steps. The first zero-field step is measurement of the starting TRM (0 Z in Figure 2). The entire remanence was imparted in the original cooling field (labeled 'Ancient Field' in Figure 2). No unblocking of the original field occurs until the 200°C Z step when a small fraction unblocks (replaced by a blue bar with no remanence).

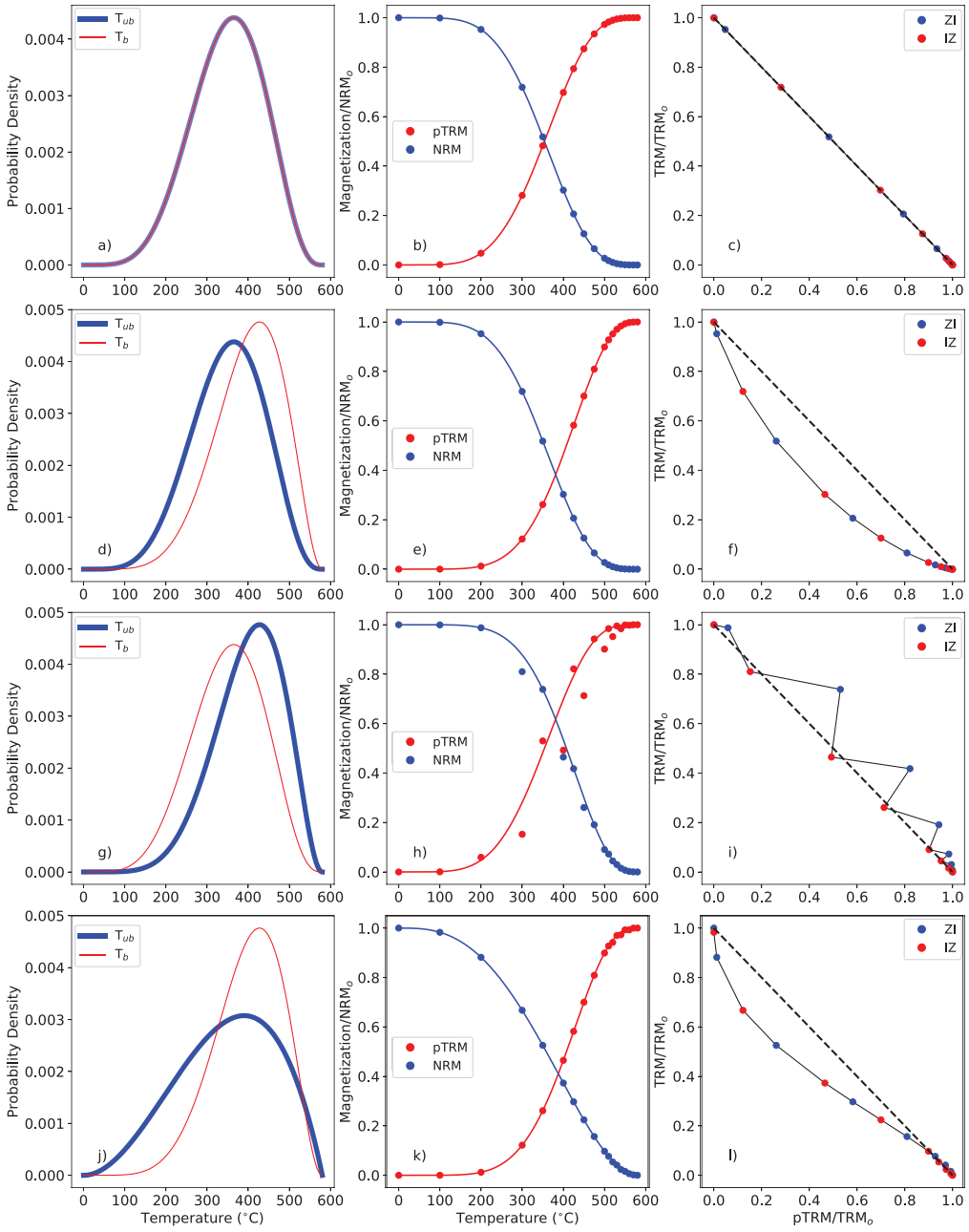

Figure 1. Phenomenological model of the effect of unequal pTRM blocking and unblocking in Arai plots. Left-hand panels: distribution of (un)blocking temperatures. Blue is the unblocking temperature (T_{ub}) spectrum and red is the blocking temperature (T_b) spectrum. Middle panels: NRM demagnetization (blue) and pTRM acquisition (red). The order in which the steps are taken alternates between pTRM acquisition (in-field cooling) first and NRM demagnetization (zero-field cooling) first. Right-hand panels: plots of TRM remaining versus pTRM gained. Data for in-field followed by zero-field (IZ) steps first are indicated as red dots; zero-field followed by in-field cooling (ZI) steps first are indicated as blue dots. Heavy dashed lines are the relationship predicted by Néel theory. a-c) blocking and unblocking temperature spectra identical (Law of Reciprocity obeyed). d-f) Unblocking temperature spectrum shifted to lower temperatures than the blocking temperatures. g-i) Unblocking temperature spectrum shifted to higher temperatures than the blocking temperatures. j-l) Unblocking temperature spectrum broader than the blocking temperature spectrum.

In the 200°C I step, some of the grains that unblocked in zero field at 200°C are remagnetized in the laboratory field (orange). The process of demagnetization (blue) and remagnetization (orange) proceeds until the entire specimen has been remagnetized in the laboratory field. The resulting Arai plot from this example is shown in Figure 1f where ZI steps are plotted as blue circles and the IZ steps as red. The relationship between blocking and unblocking temperatures and the orientation of the applied field with respect to the remanence in this example produces a curved Arai plot (Figure 1f).

Thellier's laws are only strictly true for non-interacting uniaxial single domain (SD) magnetic particles whose behavior is understood using the theory of Néel (1949, 1955). In Figure 1d-f, we show an example of a case in which the unblocking temperature spectrum (blue) is somewhat lower than the blocking temperature spectrum (red). The resulting Arai plot sags below the theoretical line (heavy dashed line Figure 1f). An alternate scenario in which the unblocking temperature spectrum is somewhat higher than the blocking temperature spectrum results in a zig-zagged Arai plot (Figure 1g-h). When the unblocking temperature spectrum is wider than the blocking temperature spectrum (Figure 1j), the Arai plot is 'S'-shaped (Figure 1l). The ultimate cause of sagging, zig-zagging, or an S-shape stems from a failure to satisfy the Law of Reciprocity where remanence can be removed at either a lower temperature than originally imparted (low-temperature pTRM tails) or at a higher temperature (high-temperature pTRM tails), respectively. In this paper, we focus on possible causes and consequences of the widely observed 'sagging' behavior in Arai plots, while ignoring the influence of chemical alteration, non-linearity in TRM response, or anisotropy effects.

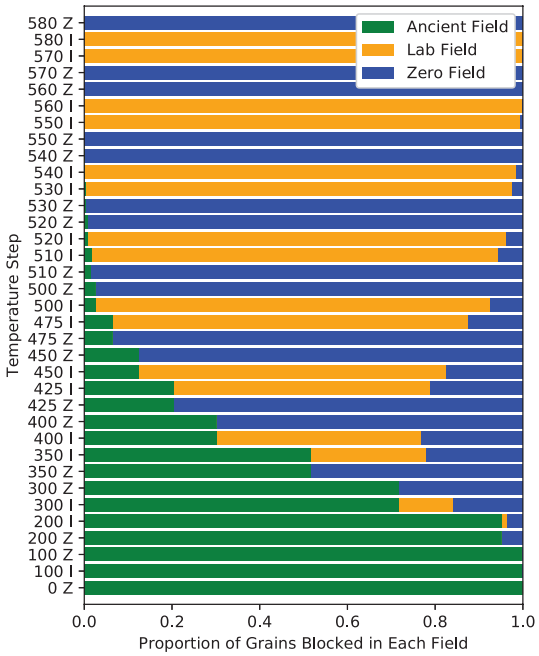

Figure 2. Example of blocking and unblocking during an IZZI experiment for the phenomenological toy model shown in Figure 1d-f. The green bars are the original TRM remaining after each heating step. The blue bars are the portion of TRM removed by cooling in zero field and the orange bars represent the portion of the remanence that was remagnetized by cooling in a laboratory field.

1.1 Sagging Arai plots in synthetic samples

Dunlop and Özdemir (2001) illustrated variable sagging in Arai plots as a function of grain size for a suite of specimens whose grains sizes were well known and likely to be multi-domain (MD). They imparted a pTRM over a narrow temperature interval (370–350°C), and thermally demagnetized them to 500°C in a step-wise fashion. The remanence remaining at each temperature step is shown in Figure 3. The heavy red line is the prediction from theory for SD particles. Clearly the Law of Reciprocity is violated by all specimens, and the larger the grain size, the larger the deviation from theory. The portion of pTRM lost by heating to below the blocking temperature is termed a 'low-temperature pTRM tail' and that above is a 'high temperature pTRM tail'. These tails have a profound effect on the outcome of double heating experiments as shown in Figure 1 where data sag below the ideal line (Figure 1f), zig-zag (Figure 1i), or are 'S'-shaped (Figure 1l).

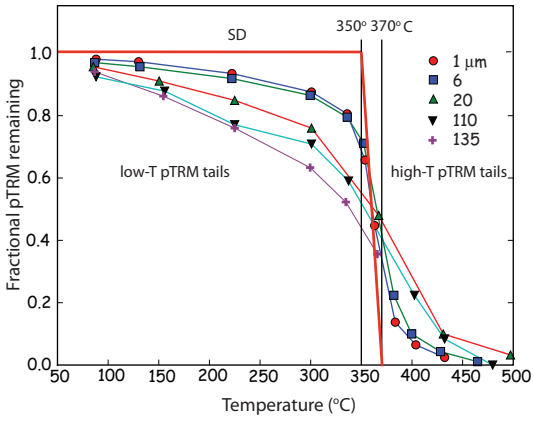

Figure 3. Stepwise thermal demagnetization of pTRMs imparted by applying a small DC field during cooling from 370 to 350°C in magnetite of known grain size. Between 50 and 90% of the remanence unblocks below (a low temperature pTRM tail) or above (a high temperature pTRM tail) the pTRM blocking temperature range. Failure of reciprocity is most extreme for the largest grain sizes. [Data of Dunlop and Özdemir (2001); figure modified from Tauxe et al. (2010).]

If a particle is large enough to be non-uniformly magnetized, e.g., in the flower or vortex magnetic states (Williams & Dunlop, 1989; Schabes & Bertram, 1988), or the multi-domain (MD) state, its magnetic behavior cannot be described by the analytical theory of Néel (1949). Just below the Curie temperature, magnetic particles are close to saturation, but as particles cool, more complex domain structures can form. In the case presented by Dunlop and Özdemir (2001), the particles were almost certainly MD and the failure of reciprocity can be understood as follows. After cooling to room temperature, a particle will have some net moment because domain walls will be distributed to produce incomplete cancellation, in equilibrium with the external field. As the temperature ramps up again, the walls shift within the particle as they seek to minimize the magnetostatic energy. If the particle is cooled back to room temperature, there could be a net magnetization loss, giving rise to the observed low temperature tails. The domain walls may not be destroyed until the temperature is near T_c and some fraction of remanence could persist, giving rise to high temperature tails.

The consequence of MD behavior is a strong bias in the resulting paleointensity estimate (Krása et al., 2003, Figure 4). Krása et al. (2003) performed KTT-type exper-

iments on carefully sized magnetite specimens ranging from SD particles of 60 nm size to ∼12 μm MD particles. The laboratory field in which the TRMs were imparted was 60 μT. Specimen MGH1 (60 nm magnetite, Figure 4a) recovered the original field with excellent accuracy (∼59 μT) while the larger grain sizes of W4 (7 μm) and W6 (12 μm) (Figure 4b and c, respectively) are increasingly biased to low values (54 and 42 μT, respectively). These data suggest strongly that MD grains should not be used for paleointensity analysis.

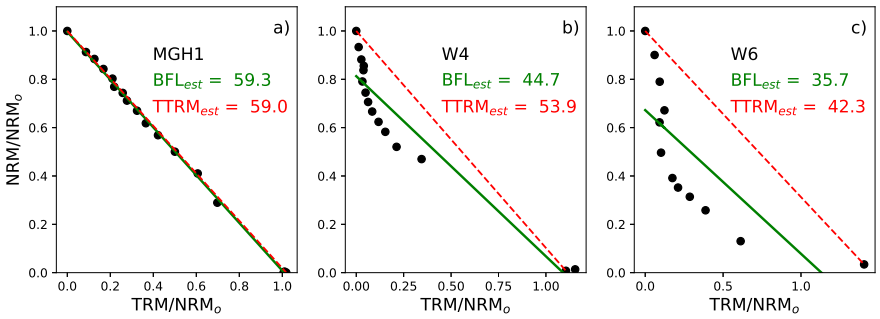

Figure 4. Examples of Arai plots for specimens with known grain sizes from Krasa et al. (2003). Magnetite with sizes: a) 23 nm, b) 7 μm, and c) 12 μm. BFL$_{est}$ is the estimated field from the best-fit heavy green lines and TTRM$_{est}$ is estimated from the total TRM (slopes of dashed red lines).

The sag (downward curvature) in the Arai plots of Krása et al. (2003) results from MD behavior, where the unblocking temperature spectrum has shifted to lower values relative to the blocking temperature (Figure 1) and the shift is caused by the resulting pTRM tails (Dunlop & Özdemir, 2001). While the existence of 'tails' has long been known (Shashkanov & Metallova, 1972), and Dunlop and Özdemir (2001) showed that MD grains have both high and low temperature pTRM tails, it is not clear that domain walls are the only cause of 'sagging' in Arai plots. Smaller non-uniformly magnetized particles without domain walls (vortex state particles) may also be responsible for tails, with unknown consequences for the success of the paleointensity experiment. Unfortunately, flower and vortex state structures (frequently referred to as "pseudo-single domain" grains after Stacey et al. (1961)) are more difficult to understand than either SD particles (which obey Néel theory) or MD particles (which are large enough for domain structures to be imaged easily, e.g. Halgedahl (1993)).

1.2 Sagging in natural samples

Many natural samples also have sagging, zig-zagging, and S-curved Arai plots. This is frequently attributed to MD behavior. Paterson (2011) developed a statistic to quantify curvature whereby $\left|\vec{k}\right|$ is the inverse of the radius of a best-fit circle. Positive values result from sagging, while negative values result from upward bowed curvature. Paterson (2011) suggested a threshold value of ±0.164 to screen for a significant MD remanence contribution. A version of the $\left|\vec{k}\right|$ statistic, modified to consider only the portion of the Arai plot used in the intensity calculation (k'), has been adopted in paleointensity experiments (e.g., Cromwell et al. (2015)) to eliminate non-linear Arai plots from paleointensity interpretations. The rationale for excluding results with significant curvature comes from empirical comparisons of 'straight' and 'curved' results from specimens that share a common field during cooling, e.g., sister specimens from the same lava flows.

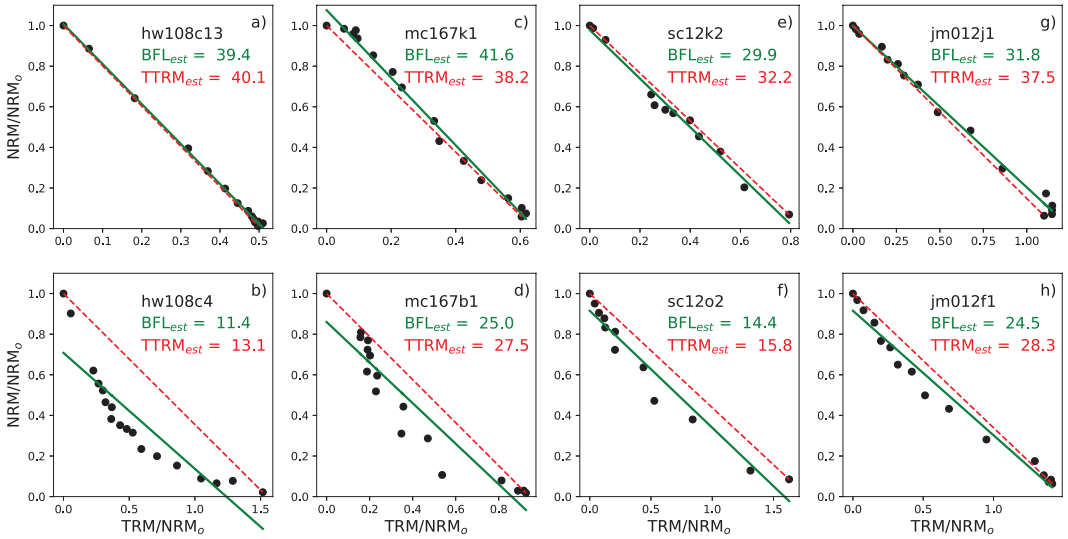

Figure 5. Examples of Arai plots for specimen pairs from the same lava flow with one 'straight' (top panel) and one 'curved' (lower panel). BFL$_{est}$ is the field intensity estimated using the best-fit line (solid green line) and TTRM$_{est}$ is that from the total TRM (dotted red line). a-b) Specimens from the 1859 lava flow on Hawaii from the data set of Cromwell et al. (2015). The IGRF estimate for the field at that time and place is 38.7 μT. c-d) Specimens from site mc167 of Lawrence et al. (2009). e-f) Specimens from site sc12 of Sbarbori et al. (2009). g-h) Specimens from site jm12 of Cromwell et al. (2013). Solid and dashed lines and intensity estimates are as in Figure 4.

Examples of pairs of specimens from the same lava flow are shown in Figure 5 for three published data sets (Cromwell et al., 2015; Lawrence et al., 2009; Sbarbori et al., 2009). In each case the estimated field strength from the specimens with curved Arai plots is lower than for those with straight Arai plots and where the ancient field is known (hw108 of Cromwell et al. (2015)), the specimen with a straight Arai plot gave an accurate answer (within <0.4 μT). Sbarbori et al. (2009) further noted that when specimen sc11e2 with a curved Arai plot (not shown) was given a laboratory TRM and the IZZI experiment was repeated, the Arai plot was straight. Investigating this 'fragile' curvature is the motivation for the present study, the first results of which were published by Shaar and Tauxe (2015).

1.3 Aging experiments for natural samples

Shaar and Tauxe (2015) investigated the evolution of Arai plot curvature over time by giving a fresh TRM to a selection of specimens whose Arai plots were curved in the original studies. The fresh laboratory TRM was then subjected to an IZZI paleointensity experiment. As seen previously, the Arai plots were much straighter than those in the original experiments; they have what we here call 'fragile curvature'. The specimens were then given another laboratory TRM and 'aged' in the same field for two years. For many specimens, the Arai plot curvature increased and the resulting intensity estimates were biased to low values relative to the laboratory field.

Santos and Tauxe (2019) built on the results of Shaar and Tauxe (2015) by adding a number of specimens whose original Arai plots were not significantly curved (see Table 1 for sampling details). They gave sets of specimens from 'straight' and 'curved' samples a fresh TRM and subjected them to an IZZI paleointensity experiment (Yu et al.,

2004; Tauxe & Staudigel, 2004) as in Shaar and Tauxe (2015). Santos and Tauxe (2019) used the k' statistic of Cromwell et al. (2015), which considers only a portion of the experimental data (as opposed to $\left|\vec{k}\right|$ of Paterson (2011)); we re-evaluate the results of Santos and Tauxe (2019) here using the original $\left|\vec{k}\right|$ statistic of Paterson (2011) (see Table 2 for values used in this study).

Locations	Lat. ($^\circ N$)	Long. ($^\circ E$)	Lithology	Age range	Citation DOI
McMurdo (mc)	-76.23	-167.43	basalt	1.26-2.28 Ma	10.1029/2008GC002072
Socorro Island (sc)	18.78	-110.98	trachyte	0.35-0.55Ma	10.1186/BF03352899
Hawaii (hw)	19.90	-155.58	basalt	1843 CE	10.1016/j.pepi.2014.12.007
Jan Mayen (jm)	71.03	-8.29	basalt	0.2-0.45 Ma	10.1002/ggge.20174
Costa Rica (cr)	9.93	-84.09	basalt	< 2 Ma	10.1002/ggge.20199

Table 1. Locations, lithologies, age ranges, and citations for samples used in the study by Santos and Tauxe (2019) and investigated here.

The behavior of the specimens in the original IZZI experiments is shown in Figure 6a-d, the 'fresh' TRMs are shown in Figure 6e-h along with the $\left|\vec{k}\right|$ statistics for each experiment, and results are summarized in Figure 7. We use here a value of $\left|\vec{k}\right| \leq 0.164$ as 'straight' (S) and values $\left|\vec{k}\right| > 0.164$ as 'curved' (C). A few specimens in the Santos and Tauxe (2019) study yielded results with significantly negative $\left|\vec{k}\right|$ values (bowed upward), which are not the focus of the current investigation. Santos and Tauxe (2019) found four categories of behavior based on a comparison of Arai plot curvature in the original versus 'fresh TRM' plots (Figures 6, 7, Table 2).

1. S-S behavior in which Arai plots for both the original NRM (Figure 6a) and the 'fresh' laboratory TRM (Figure 6e) were classified as 'straight' (S); these comprise the SS group in Figure 7.
2. S-C behavior in which Arai plots for the original NRM (Figure 6b) was 'straight', but the 'fresh' laboratory TRM (Figure 6f) was curved (C); these comprise the SC group in Figure 7. This behavior results from the high temperature 'hook' which was not well expressed in the original experiments owing to differences in experimental design.
3. C-S behavior in which original Arai plots were 'curved' (Figure 6c) but the fresh TRMs (Figure 6g) were straight (the CS group in Figure 7).
4. C-C behavior in which the original Arai plot was 'curved' (Figure 6d) and the fresh TRM was also curved, although in all cases less than the originals (Figure 6h); these are the CC group in Figure 7.

For C-S and C-C behaviors, all of the 'fresh' TRM results are straighter than in the original experiments, as described by Sbarbori et al. (2009), but the C-S samples became 'straight' as quantified with the curvature criterion of Paterson (2011) while the C-C samples remained significantly curved. We know from Dunlop and Özdemir (2001) and Krása et al. (2003) (among others) that MD-dominated samples have significant curvature even for freshly imparted TRMs (Figure 4). The curvature in our natural samples (C-S and C-C) is not reproducible in the fresh TRMs and is not explained easily by MD behavior alone. We call this behavior 'fragile' curvature.

Several questions regarding this 'fragile' (as opposed to the reproducible curvature of MD grains) spring to mind.

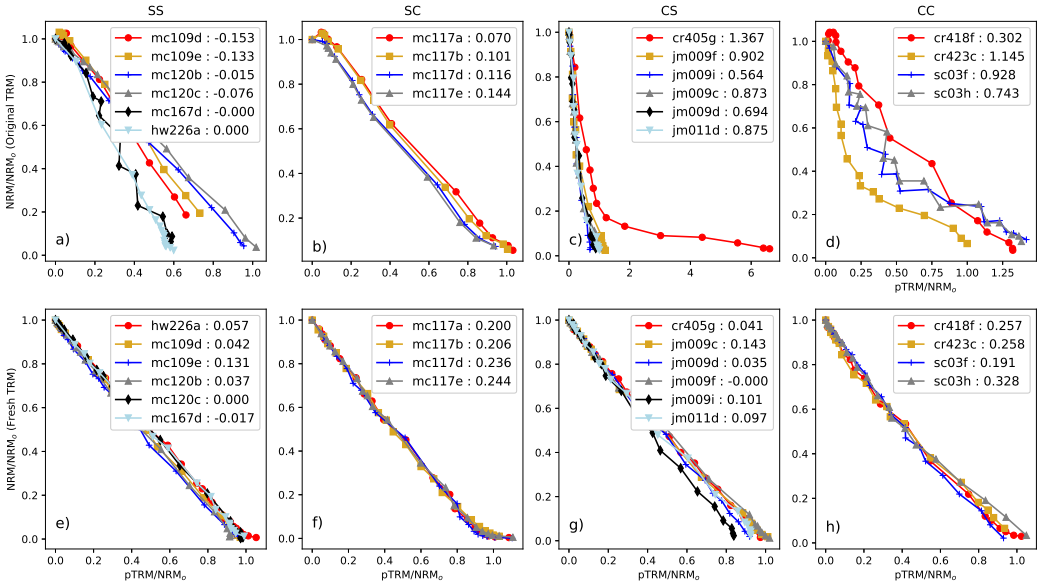

Figure 6. Arai plots for specimens from Santos and Tauxe (2019) and references therein. a, e) S-S behavior; b, f) S-C behavior; c, g) C-S behavior; and d, h) C-C behavior. Top row: Arai plots from the original studies. Bottom row: same as top row, but for the fresh TRM experiments of Santos and Tauxe (2019).

- Does fragile curvature develop over time as suggested by Shaar and Tauxe (2015)?
- Are paleointensity estimates from Arai plots with fragile curvature generally biased (as are results from MD dominated curvature)?
- Does curvature increase depend on the strength of the aging field?
- Do paleointensity estimates from Arai plots with fragile curvature depend on orientation of aging field?
- What causes fragile curvature?

To address these issues, we subjected sister specimens from the samples investigated by Santos and Tauxe (2019) (see Table 1) to extensive hysteresis experiments and an 'aging' experiment, similar to that described by Shaar and Tauxe (2015), but with some modifications. We describe below the experimental details, summarize the results, and consider the questions raised above concerning the temporal stability of fragile curvature and its effects on our ability to estimate ancient field strength.

2 Methods

2.1 Magnetic hysteresis

As part of their rock magnetic characterizations, Santos and Tauxe (2019) measured hysteresis loops for specimens from all samples studied. They plotted so-called 'Day plots' (Day et al., 1977) and estimated the bulk domain stability (BDS) parameter of Paterson et al. (2017). The latter is listed in Table 2 along with the curvature values of the original and laboratory (fresh) TRMs.

First-order reversal curve (FORC) diagrams (Pike et al., 1999) are often used to provide information about domain states, so we subjected specimens from each sample studied by Santos and Tauxe (2019) to the xFORC hysteresis protocol of Zhao et al. (2017)

Sample	$\vec{k}_{orig}$	$\vec{k}_{fresh}$	T	BDS	T/R	σ	Lobes	W	FWHM	NPF	APF
mc167d	-0.0000	-0.0173	SS	0.29	0.3427	0.1126	NPN+	61	8	5.52	25.6
mc120c	-0.0761	0.0000	SS	0.67	0.0834	0.0239	NPN+	46	10	7.53	26.61
mc120b	-0.0149	0.0368	SS	0.64	0.0787	0.0371	NPN	65	13	6.53	37.65
mc109e	-0.1330	0.1313	SS	0.43	0.1876	0.0808	NPN+	53	5	4.52	17.57
mc109d	-0.1529	0.0422	SS	0.46	0.1534	0.049	NPN+	105	12	5.52	28.61
hw226a	0.0000	0.0566	SS	0.72	0.07	0.0509	-	89	24	0.5	46.69
mc117e	0.1438	0.2439	SC	0.40	0.2393	0.09	NPN+	55	1	5.52	20.58
mc117d	0.1164	0.2357	SC	0.36							
mc117b	0.1010	0.2060	SC	0.39	0.2533	0.0797	NPN+	53	8	4.52	21.59
mc117a	0.0700	0.1997	SC	0.36	0.3659	0.1022	NPN+	81	11	7.53	32.63
jm011d	0.8755	0.0969	CS	0.45	0.2636	0.0829	NPN+	94	14	8.53	37.65
jm009i	0.5640	0.1011	CS	0.41	0.2435	0.0698	NPN+	138	10	9.54	38.65
jm009f	0.9016	-0.0000	CS	0.41	0.2967	0.0861	NPN+	184	21	10.54	60.74
jm009d	0.6936	0.0354	CS	0.41	0.2419	0.0808	NPN+	141	9	7.53	32.63
jm009c	0.8729	0.1434	CS	0.38	0.395	0.1248	NPN+	234	15	11.55	53.71
cr405g	1.3667	0.0409	CS	0.16	0.2268	0.0962	NPNPN	125	5	5.52	27.61
sc03h	0.7425	0.3277	CC	0.53	0.1234	0.0378	NPNPN	77	5	5.52	31.63
sc03f	0.9284	0.1905	CC	0.44	0.157	0.0472	NPN+	61	4	5.52	18.57
cr423c	1.1446	0.2575	CC	0.31	0.2837	0.1172	NPNPN	148	21	9.54	34.64
cr418f	0.3018	0.2567	CC	0.27	0.4134	0.1349	NPNPN	151	20	6.53	32.63

Table 2. Summary of statistics and parameters for samples used in this study. $\vec{k}_{orig}$: $\vec{k}$ statistic for the original data recalculated from references cited in Table 1. $\vec{k}_{fresh}$: $\vec{k}$ statistic for paleointensity data from fresh TRMs (recalculated from Santos and Tauxe (2019)). T: Type of curvature for aged versus fresh $|\vec{k}|$ statistic of Paterson (2011) where 'S' is 'straight' with $|\vec{k}| \leq 0.164$ and 'C' is ''curved' with $|\vec{k}| > 0.164$. BDS is the bulk domain stability parameter of Paterson et al. (2017) as reported by Santos and Tauxe (2019). T/R: ratio of the tFORC and remFORC integrated over FORC Zones 1 and 3, respectively. σ: standard deviation of T/R. Lobes: number and sign of iFORC lobes where N = negative and P = positive (see Figure 8). Width: width of FORC distribution along the B_i axis (mT). FWHM: full-width half-maximum value (mT). NPF: Nucleation peak field (mT). APF: Annihilation peak field (mT).

at the Australian National University, Canberra, Australia. Representative conventional FORC diagrams (Pike et al., 1999), and remanence FORC (remFORC), transient FORC (tFORC), and induced FORC (iFORC) diagrams of Zhao et al. (2017) for each of the four categories of interest are shown in Figure 8 with plots generated using the xFORC software available at: https://sites.google.com/site/irregularforc/. We used the 'irregular FORC' measurement protocol of Zhao et al. (2015) and plots were generated with smoothing factors (SF) as noted in the figure caption. The tFORCs are the difference between the conventional FORC (left-hand panel in Figure 8) and the transient-free FORC (tfFORC, not shown) while the iFORCs are the difference between the conventional FORC and the remFORC (panel second from left in Figure 8). The iFORCs in our experiments have several lobes of negative or positive coercivities (labeled N or R in Figure 8d, h, l, p). In many of our samples, the negative lobe in Zone 1 (e.g., Figure 8h, l) has two parts. These are labeled 'N+' in Figure 8 and Table 2.

There are several ways of characterizing and quantifying aspects of FORC diagrams. One, as described by Carvallo et al. (2006), is to the plot the width of the coercivity spectrum along the B_i axis, against the full-width half-maximum value (FWHM) for a profile through the peak of the coercivity distribution. The width provides a measure of the

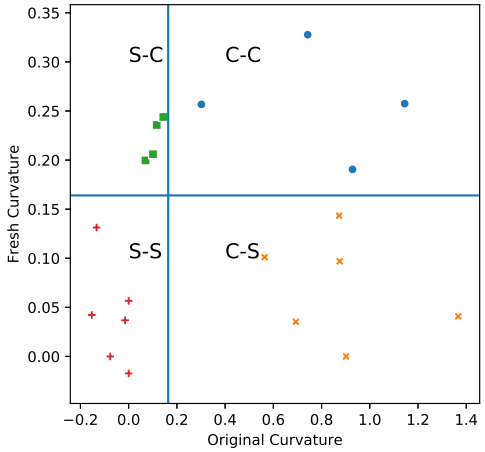

Figure 7. Comparison of curvature as quantified by $\vec{k}$ for the fresh TRMs of Santos and Tauxe (2019) versus original TRMs (see Table 1 for references). Specimens from samples with low curvature (S) either remained straight (SS) or became significantly curved (SC) after being given a fresh TRM. Specimens from samples with high curvature (C) either became straight (CS) or remained curved (CC) after being given a fresh TRM. All CC specimens have significantly less curved Arai plots than in the original experiments, so they have 'fragile' curvature.

non-SD content of the specimen, and FWHM provides a measure of the interaction field distribution for SD grains. Width and FWHM values for specimens measured in this investigation are listed in Table 2.

Another way to characterize FORC behavior is to consider the relationship between fields at which vortices nucleate and are annihilated as described by Novosad et al. (2001). The transient nature of vortex structures is what gives rise to so-called 'transient hysteresis' (e.g., Fabian, 2003; Yu & Tauxe, 2005). From results for FeNi nanodots (Novosad et al., 2001), both the nucleation peak field (NPF) and annihilation peak field (APF) depend strongly on grain size with smaller particles having larger nucleation and annihilation fields, and the APF is larger (in the absolute sense) than the NPF. Estimates of nucleation and annihilation fields from the marginal field distributions in the tFORC diagram are illustrated in Figure 9 and peak fields are listed in Table 2.

A third way of quantifying FORC behavior is to calculate the ratio of transient hysteresis to remanence hysteresis by integrating the FORC response over Zone 1 of the tFORC diagram and that of Zone 3 of the remFORC diagram. The latter is dominated by SD grains while the former is dominated by larger grains with transient hysteresis behavior. This ratio (T/R) should reflect the concentration of grains with transient hysteresis behavior (vortex and/or MD magnetic grains) relative to SD grains. We list values of T/R with uncertainties in Table 2.

2.2 Aging and IZZI experiments

Ten sister specimens of the same samples used by Santos and Tauxe (2019) were given a fresh TRM in a laboratory field of 70 μT as in Santos and Tauxe (2019). Instead of subjecting them immediately to the paleointensity experiment, they were allowed to age for two years in laboratory fields of either 35 or 70 μT in five orientations: parallel to the field used to impart the fresh TRM (Pos 1), or at increasingly large angles (Pos

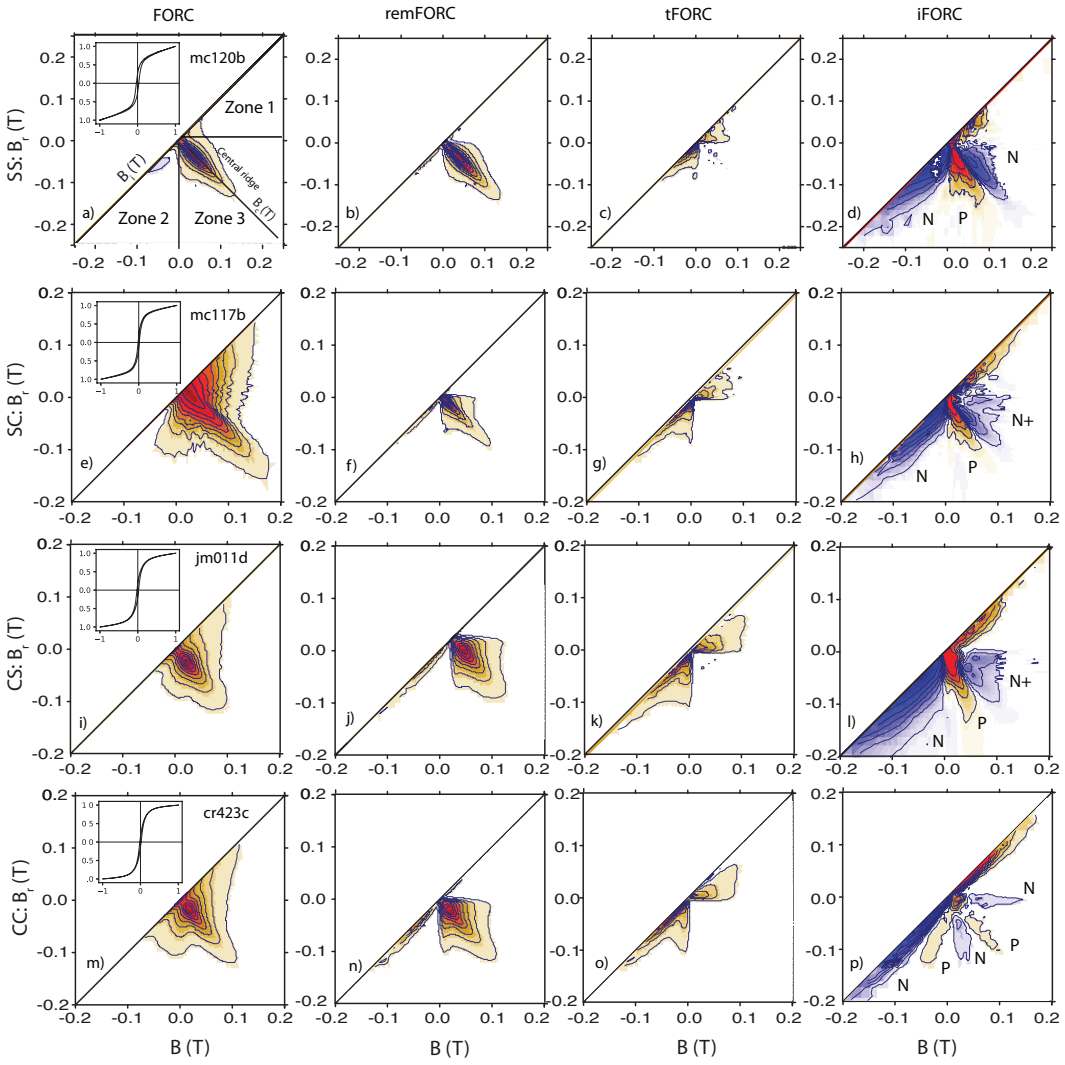

Figure 8. Representative FORC diagrams for samples from the four categories of behavior. Smoothing factor (SF) = 2 for all FORCs, remFORCs, and tFORCs. SF = 3 for all iFORCs except mc120d for which SF = 4. The non-linear color scale factor was 1 for all plots except the iFORCs, which were set to 10. a-d) Specimen from S-S sample mc120b. e-h) Specimen from S-C sample mc117b. i-l) Specimen from C-S sample jm011d. m-p) Specimen from C-C sample cr423c. Left-hand panels: conventional first-order reversal curve (FORC) diagrams; insets are the major loops (magnetization (M/M_{max}) versus field (T)). Second panel from left: remanence FORC (remFORC) diagrams. Second panel from right: transient FORC (tFORC) diagrams. Right-hand panels: induced FORC (iFORC) diagrams.

2 - Pos 5) in Figure 10. We consider results from Positions 1, 3, and 5 in this paper; the other positions were reserved for other ongoing experiments. After aging for two years, each specimen from positions 1, 3, and 5 in the two laboratory fields of 35 and 70 μT were subjected to the IZZI experiment.

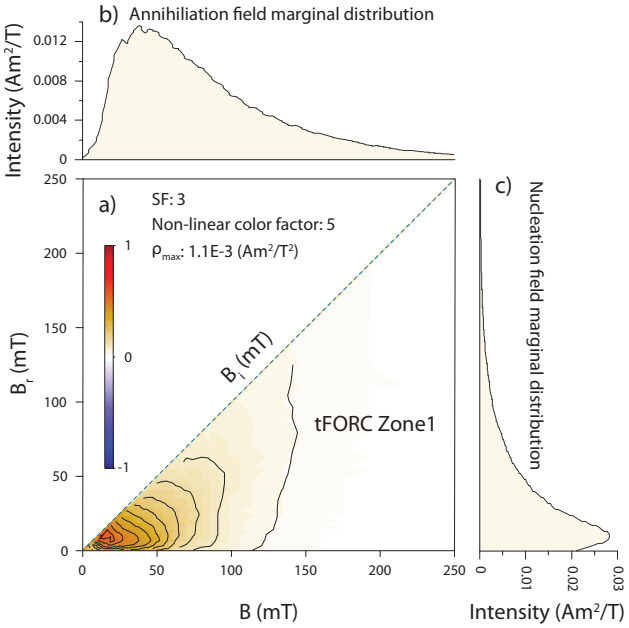

Figure 9. Example of marginal distribution of nucleation and annihilation fields from Zone 1 of the tFORC distribution. a) Zone 1 of the tFORC distribution for sample jm011d. b) and c) Marginal distributions of the annihilation and nucleation fields, respectively. The smoothing factor (SF) and non-linear color scale for the FORC diagram are specified.

3 Results

3.1 FORCs

Representative FORC diagrams are shown in Figure 8. We also list the values of various hysteresis parameters considered in this investigation in Table 2.

The S-S specimen from sample mc120b has dominantly SD behavior (Figure 8a) with a prominent 'central ridge' (Zone 3) and closed FORC contours that are characteristic of non-interacting uniaxial SD populations (Roberts et al., 2000; Egli et al., 2010). Non-interacting SD grains should also have no transient hysteresis (Yu & Tauxe, 2005; Fabian, 2003; Zhao et al., 2017; Harrison et al., 2019), which is consistent with the subdued tFORC signal (Figure 8c). The remFORC diagram (Figure 8b) is similar to the conventional FORC diagram, except that the conventional FORC diagram has a negative lobe along the lower left-hand axis (Zone 2), which is also characteristic of uniaxial SD particles (Muxworthy et al., 2004; Newell, 2005; Egli et al., 2010).

In contrast to the S-S example, the C-C specimens (e.g., from sample cr423c; Figure 8m-p) have no negative lobe associated with uniaxial SD particles in Zone 2 of the FORC diagram (Figure 8m). The conventional FORC diagram for this specimen has a tri-lobate 'pirate hat' shape associated with multi-vortex (MV) behavior (Lascu et al., 2018). The tFORC distribution has distinctive lobes (Figure 8o) and the iFORC diagram (Figure 8p) has five lobes (NPNPN). The lobate tFORC distribution and the NPNPN iFORC lobe structure are manifestations of vortex state behavior (Zhao et al., 2017). The wide distribution along the B_i axis is also associated with coarse magnetic grain sizes. We list the width as estimated by Carvallo et al. (2006) in Table 2. We interpret the CC series of FORC diagrams as indicative of dominantly coarse grain sizes in the large vor-

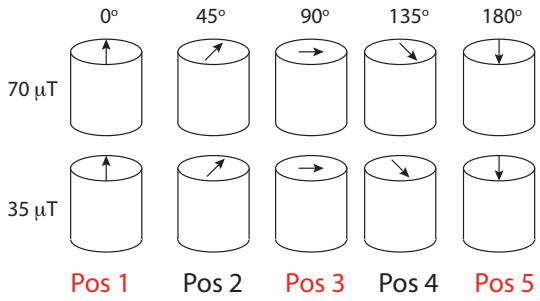

Figure 10. Design of the aging experiment. Sister specimens for each sample from Santos and Tauxe (2019) were given a fresh TRM along the direction of the arrows in a laboratory field of 70 μT. Specimens were placed in one of five positions (Pos 1- Pos 5) in either a 70 μT or 35 μT field.

tex size range (including 'bent' single vortex structures and multi-vortex domain states and perhaps also a MD component).

S-C specimens (e.g., mc117b in Figure 8e-h) have elements in common with both S-S samples (e.g., FORC central ridge; Figure 8e) and C-C samples (e.g., lobed tFORC feature; Figure 8g). The iFORC diagram (Figure 8h) has three lobes compared to the five in the C-C samples and the width along the B_i axis is not nearly as large as for the C-C sample (see Figure 8m and Table 2). Thus, the FORC behavior of such specimens is indicative of SD to vortex state behavior, with most of the remanence carried by SD grains (Figure 8f). Hints of MD behavior are suggested by negative cooling rate corrections for some specimens (Santos & Tauxe, 2019), which are usually associated with domain walls.

C-S specimens (e.g., jm011d in Figure 8i-l) also have elements in common with both the S-S samples and the C-C samples. The FORC distribution along the B_i axis is even wider than for cr423c (Figure 8m, Table 2) and the tFORC diagram (Figure 8k) has 'wings' rather than the lobate structure in Zone 2 that is observed for both the S-C and the C-C samples, both of which suggest a significant contribution from coarse magnetic grains. In contrast, the iFORC diagram (Figure 8l) has only the three lobes (negative-positive-negative), which are indicative of SD behavior (Zhao et al., 2017; Harrison et al., 2019). Interestingly, the negative lobe in Zone 1 also has two 'wings'. We term these features, NPN+ in Table 2. We interpret the FORC results as indicating a broad distribution of SD to large vortex or perhaps even MD grain sizes.

The Carvallo plot (Carvallo et al., 2006) shown in Figure 11a suggests that none of the samples investigated here have FWHM values in excess of the threshold value of 29 mT, which might be expected to cause paleointensity experiments to fail because of strong magnetostatic interactions. Six samples have width values in excess of the 132 mT threshold value that might be expected to cause failure of paleointensity experiments because of non-SD magnetic behavior. All of these samples have either C-C or C-S behavior with 'fragile curvature'. The specimen from sample cr405g also has C-S behavior and width close to the threshold value.

A plot of annihilation peak field versus nucleation peak field (Figure 11b) has a single outlier (hw226a), while data from other specimens appear to be related linearly to each other, as expected for vortex nucleation and annihilation. A FORC diagram for hw226a (Figure 12) is different from the other FORC diagrams (e.g., Figure 8). It has a strong central ridge along the B_c axis that is characteristic of SD grains. The respective rem-

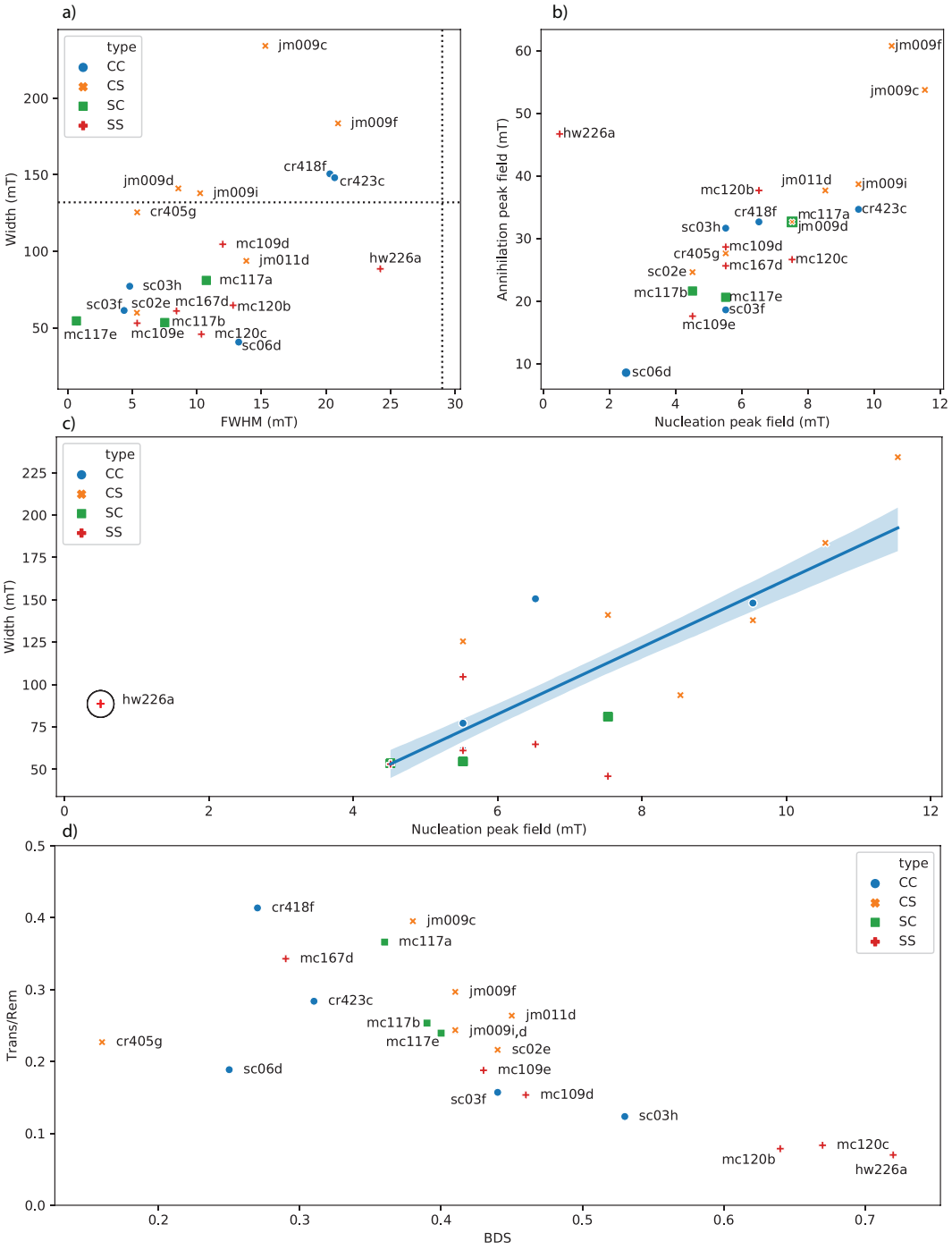

Figure 11. a) A 'Carvallo plot' (Carvallo et al., 2006) with width of the FORC distribution along the B_i axis plotted against the full-width half-maximum (FWHM) of a vertical profile through the peak of the coercivity distribution. Threshold values recommended by Carvallo et al. (2006) for FWHM and width are 29 mT and 132 mT, respectively. No samples exceed the FWHM threshold, but all specimens that exceed the width threshold are sisters of CS or CC type samples. b) Annihilation peak field (APF) versus nucleation peak field (NPF). c) Width versus nucleation peak field (NPF). Best-fit line with bootstrap uncertainty bounds were calculated without including data for specimen hw226a. d) Trans/Rem ratio (T/R in Table 2) plotted against bulk domain stability (BDS in Table 2).

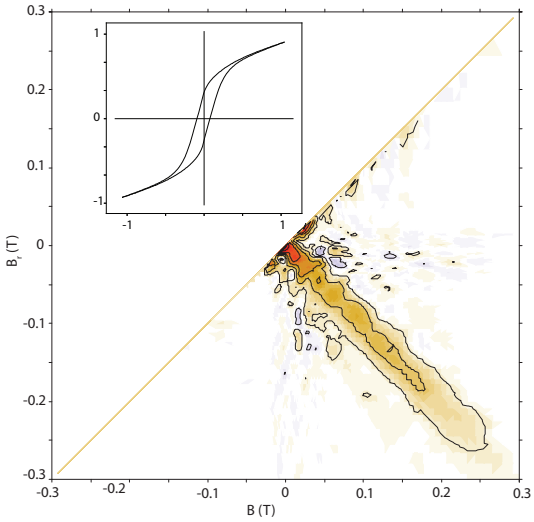

Figure 12. Conventional FORC diagram for hw226a. Smoothing factor = 3; Non-linear color scale factor = 2. See description in the Figure 7 caption for the left-hand panel.

FORC diagram (not shown) is nearly identical and there is little transient or induced behavior (also not shown). This sample, a quenched flow top from Hawaii, is perhaps the best example of SD dominated behavior among the samples studied here.

We plot the width parameter (Carvallo et al., 2006) against NPF in Figure 11c. There is a quasi-linear relationship between the two, apart from hw226a, which is again an outlier. All samples, apart from hw226a, have behavior characteristic of non-SD behavior with significant transient hysteresis. The fact that the sole truly SD sample (hw226a) has the lowest NPF value among the samples reflects the lack of vortex state particles in this sample.

Both BDS (Paterson et al., 2017) and the T/R statistic proposed here are meant to characterize domain state. To compare the two, we plot the T/R ratios listed in Table 2 against BDS values estimated for sister specimens by Santos and Tauxe (2019) in Figure 11d. Apart from cr405g and sc06d, there appears to be an inverse relationship between the two parameters, with higher BDS values associated with lower transient hysteresis. It also appears that the C-S samples are shifted to higher T/R values with similar BDS values than the S-C or C-C samples. Higher BDS values result from higher saturation remanence to saturation magnetization, with values closer to one thought to represent more SD-like behavior. It, therefore, makes sense that higher BDS values are associated with lower transient hysteresis.

3.2 Aging

Results for all IZZI experiments on aged specimens are shown in Figure 13. All but two of the 36 aged specimens in the S-S category have $\left|\vec{k}\right| \leq 0.164$ and are 'straight' based on that criterion. The two exceptions are specimens from mc109e (mc109e-SB3) and hw226a (hw226a-SB5), which appear to have altered during the experiment as indicated by a remanence vector that bypasses the origin and grows into the direction of the laboratory field (e.g., Figure 14a). These specimens are not discussed further.

In the S-C group, results vary strongly as a function of aging position. For position 5 (aging field antiparallel to the cooling field), none of the eight specimens became significantly curved after aging but for position 1 in the 70 μT aging field all but spec-

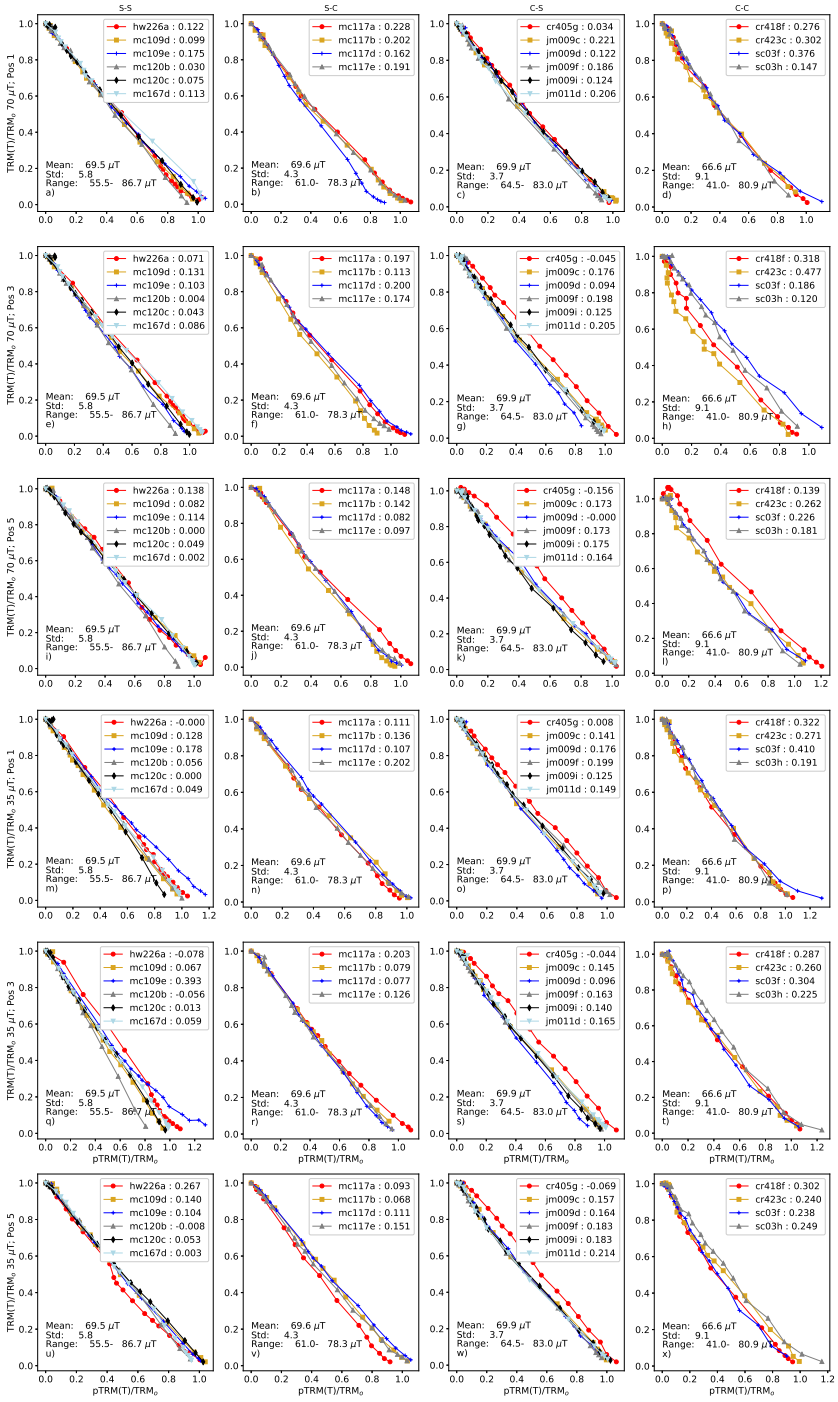

Figure 13. Results of aging experiments. Columns are from left to right: S-S, S-C, C-S, and C-C. Rows are results from different aging conditions. From top to bottom these are: 70 μT, Position 1; 70 μT, Position 3; 70 μT, Position 5; 35 μT, Position 1; 70 μT, Position 3; and 70 μT, Position 5. The legends are the names of the samples from which the specimens were taken and the values of $|\vec{k}|$.

414 imen mc117d-SA1 became significantly curved. However, for the 35 μT aging field, all

but one specimen (mc117e) stayed straight. The different behaviors for the different aging conditions may be influenced strongly by inter-specimen variability within the same samples, which all come from the same lava flow (mc117).

In the C-S group, Arai plots for three of the six specimens aged in the 70 μT field (jm009c, jm009f, and jm011d) became curved in all three positions, while the others remained straight. The Arai plot for a specimen from jm009i also became curved in position 5. Although not significant, the Arai plot for a specimen from cr405g acquired a slight up-bowing in this field, which implies acquisition of a slight but stable viscous remanent magnetization (VRM) (Figure 14b). In the 35 μT aging field in position 1, Arai plots for jm009d and jm009f both became curved. In position 3, only the Arai plot for specimen jm011d became curved. In position 5, all Arai plots except for those for cr405g and jm009c (of the six specimens) became curved.

In the C-C group, the Arai plot for sc03h was straight in positions 1 and 3 at 70 μT; the Arai plot for cr418f was straight in position 5. This specimen (cr418f-CA5) appears to have acquired a VRM parallel to the magnetizing field (antiparallel to the NRM), which was only removed by about 350°C (Figure 14c). All other Arai plots remained curved.

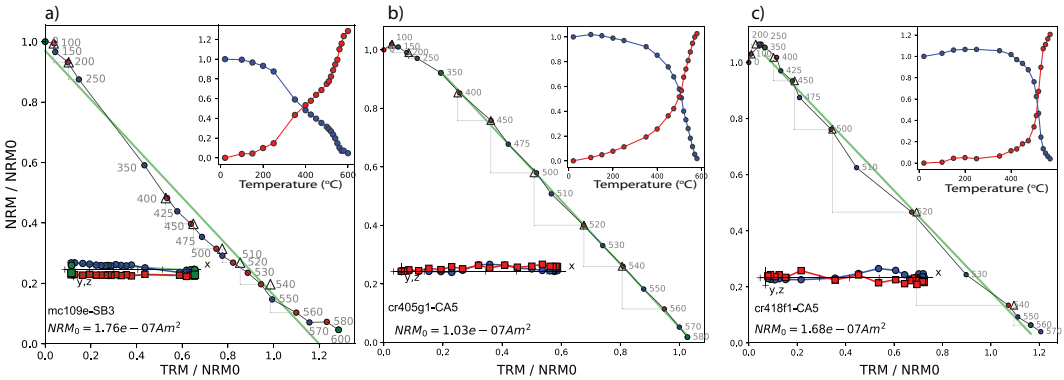

Figure 14. Unusual behavior during the IZZI experiment. Arai plots with best-fit line in green. ZI (IZ) steps are plotted as blue (red) circles; pTRM check steps are plotted as triangles. Lower left insets: Zijderveld (1967) diagrams of remanence decay. X-Y (X-Z) projection plotted as blue circles (red squares). Upper right insets: remanence decay (acquisition) plotted as blue (red) symbols. a) Specimen altered during the experiment. b-c) Specimens acquired a VRM during aging in a 70 μT field anti-parallel to the NRM. The plots were made with thellier_gui.py in the PmagPy software package of Tauxe et al. (2016).

4 Discussion

4.1 Does fragile curvature grow over time?

To investigate whether curvature grows over time, we compare in Figure 15 data from Santos and Tauxe (2019) (light colored bars) with curvature from the aged specimens investigated here (darker bars). In the C-C group, all but the six specimens from sc03h have larger curvature after aging than when fresh. In the C-S group, all but the cr405g specimens have higher curvature in the aged group. Specimens from cr405g instead have negative curvature (upward bowing), which is due to a form of VRM (Figure 14) that is more stable than expected from Néel (1949) theory. According to Pullaiah et al. (1975), a VRM acquired over a few years should be removed by thermal demagnetization to 150°C, but it is not removed until ∼300°C here. In the S-S group, five of

six samples (30 specimens) have enhanced curvature, although all except one (hw226a-SB5) remained straight. The exception to the overall increased curvature after aging occurs in the S-C group. All but one specimen had decreased curvature after aging.

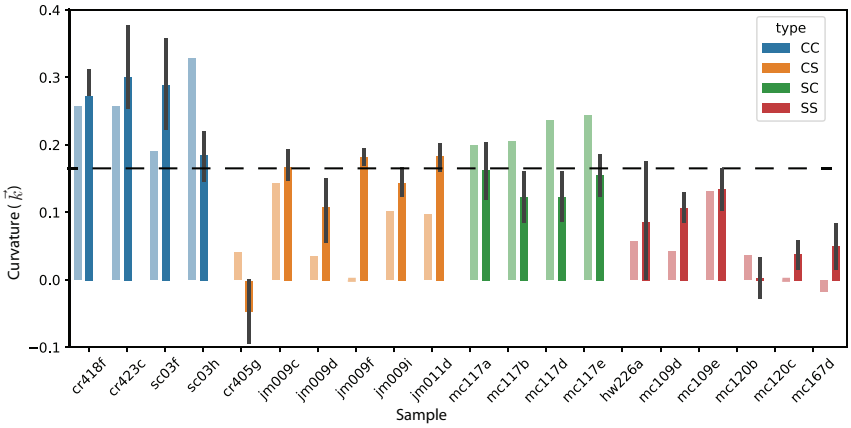

Figure 15. Curvature parameter $\left|\vec{k}\right|$ for fresh (lighter colored) versus aged (darker colored) specimens.

We replot the data from Figure 15 in Figure 16a and include results from Shaar and Tauxe (2015) (reinterpreted in a consistent manner with the present study) in Figure 16d. In both data sets, the curvature in Arai plots for aged specimens (except for the S-C group) is more positive than in fresh specimens. Shaar and Tauxe (2015) stated that curvature increases when specimens are aged in a laboratory field identical to the original cooling field (which is inconsistent with predictions from Néel (1949) theory). Here, we repeated the experiment with different aging field strengths and directions relative to the fresh TRM, with similar results. Therefore, we take these data to demonstrate that fragile curvature in most lava specimens relevant to absolute paleointensity analysis generally increases through time regardless of aging field strength or direction.

4.2 Are paleointensity estimates from fragile curvature biased?

Using intensities estimated from total TRMs, we plot kernal density estimates for fresh and aged specimens in Figure 16b. Estimates from the 'straight' results (both fresh and aged) are unbiased with average values of 71 and 70 μT, respectively. This contrasts with results from fresh and aged curved experiments, which have average values of 65 and 67 μT, respectively. The results, including those from Shaar and Tauxe (2015), which were aged as in our position 1 in a 70 μT field, are shown in Figure 16e. In the combined data set, average values for fresh and aged 'straight' TRMs are 67 and 69 μT and those for curved fresh and aged TRMs are 65 and 67 μT, respectively. These results support the hypothesis that curved Arai plots tend to yield intensity estimates that are biased low, while straight Arai plots tend to be more accurate. They also validate the use of the curvature criterion proposed by Paterson (2011) as a useful criterion for evaluating paleointensity data. In both data sets, estimates from curved aged specimens are more accurate than from fresh TRMs perhaps because of the increased specimen numbers or a dependence of the paleointensity estimate on direction of the aging field (aging in anti-parallel fields results in less bias for unknown reasons).

Finally, we investigated the role of the angle of the aging field. We plot intensities for the aged groups as a function of aging field orientation in Figure 16c, with the data of Shaar and Tauxe (2015) (which were only in position 1) included in Figure 16f. There

is a subtle shift to both wider distributions and lower intensities when aged in an orthogonal field (position 3); thus, both accuracy and precision are affected.

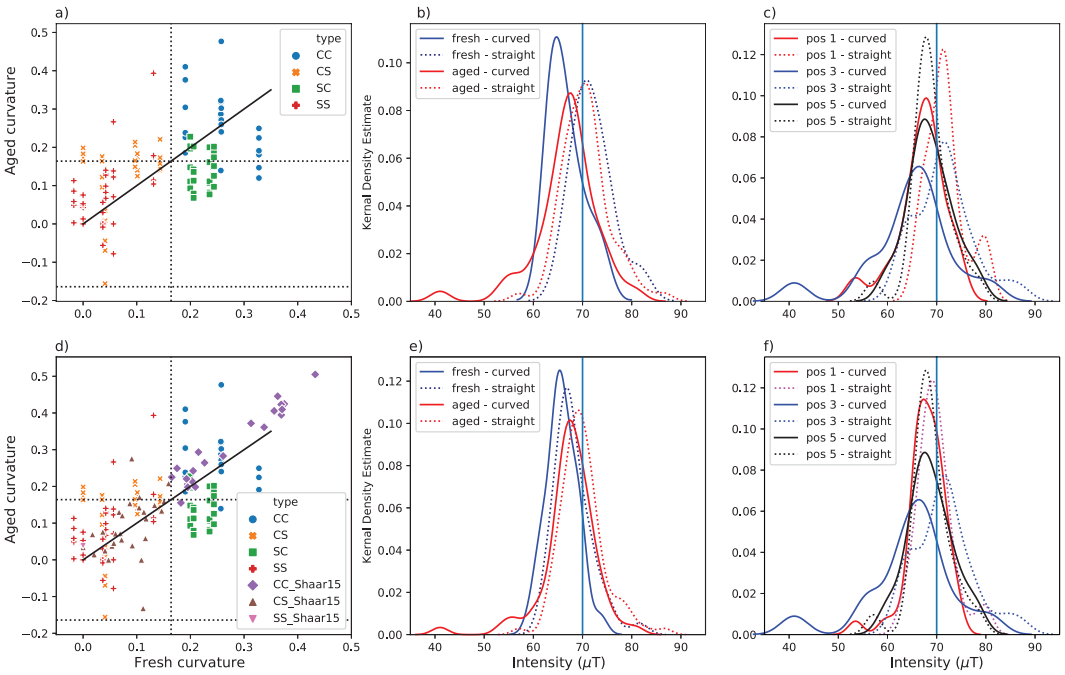

Figure 16. a) Comparison of results for aged versus fresh curvature in Arai plots. b) Kernal density estimates of intensity estimates for fresh (aged) specimens in blue (red) solid lines. Dotted lines are estimated intensities after removing results with $\left|\vec{k}\right| > 0.164$. c) Intensity estimates as a function of aging experiment. d-f) Same as a-c), but including results from Shaar and Tauxe (2015).

4.3 What causes fragile curvature?

MD grains give rise to curved Arai plots, but the curvature is reproducible in fresh TRMs. What we see here is first a disappearance of curvature in fresh TRMs compared with the original TRMs, followed by growth of curvature over time. Curvature is produced by unequal blocking temperatures relative to unblocking temperatures (Figure 1). When the unblocking temperature spectrum of the TRM is lower than the blocking temperature spectrum, the result is a downward curvature (sag) of the associated Arai plot and positive $\vec{k}$. Alternatively, when the unblocking temperature spectrum of the TRM is higher than the blocking temperature spectrum, the IZZI experiment does not produce upward curvature of the associated Arai plot; rather, there is a pronounced 'zig-zag', as described by Yu et al. (2004). Downward curvature results from low temperature pTRM tails and the zig-zag from high-temperature pTRM tails (Figure 1).

Much progress has been made with micromagnetic modeling (e.g., Williams and Dunlop (1989); Schabes and Bertram (1988); Fabian et al. (1996); Tauxe et al. (2002); Nagy et al. (2017); Fabian and Shcherbakov (2018)). Nagy et al. (2017) suggested, astonishingly, that equidimensional magnetite particles with single vortex (SV) magnetic structures are even more stable paleomagnetically that SD particles. Furthermore, a region exists between the so-called 'flower" and "vortex" states (Schabes & Bertram, 1988; Williams & Dunlop, 1989), in which the vortex axis is aligned with the magnetocrystalline 'hard' direction. In this region, relaxation τ (related to the rate of 'flipping' between di-

rections associated with magnetic energy minima) drops precipitously from longer than the age of the Earth to about a year with a related blocking temperature drop from over 400°C to about 100°C. This is precisely the blocking temperature interval involved in the 'aging' process described here, where blocking temperatures appear to have shifted to higher values in Earth-like fields over two years. It is, therefore, plausible that fragile curvature results from a blocking temperature migration in or near the low stability grain sizes to more stable states.

The suggestion that fragile curvature is related to unstable domain states is supported by information gleaned from FORC diagrams. All samples with width parameters that exceeded the threshold values proposed by Carvallo et al. (2006) had original Arai plots that were significantly curved (and subsequently became much straighter when given a fresh TRM in the laboratory). However, data for some of these C-C or C-S type samples fall below the threshold. Moreover, all S-S type samples had either no induced magnetization component (hw226a) or a NPN(+) iFORC structure (as opposed to NPNPN structures, see Table 2). Similarly, all but one (sc03f) of the C-C samples had five-fold lobate structure (NPNPN) in their iFORC diagrams. All S-C samples were like many of the S-S samples in that they had NPN+ iFORC structures as did all but one of the C-S samples (cr405g) which had the NPNPN structure. In general, the best predictor of curved Arai plots appears to be the NPNP iFORC structure that is strongly associated with the fragile curvature phenomenon.

5 Conclusions

1. There is a distinct difference between the curvature in Arai plots that results from MD behavior (e.g., Dunlop and Özdemir (2001); Krása et al. (2003)) and the 'fragile' curvature described by Shaar and Tauxe (2015) and Santos and Tauxe (2019). The former is reproducible in the laboratory while the latter largely disappears when specimens are given a 'fresh' TRM.
2. Curved Arai plots for MD grains are severely biased with significantly lower than expected intensity estimates for known laboratory fields (Krása et al., 2003).
3. Results for specimens with 'fragile' curvature are also biased to low values relative to straight Arai plots from the same cooling units.
4. Arai plots for specimens with fragile curvature tend to become more curved when given a fresh TRM and allowed to 'age' in controlled laboratory fields.
5. Results for specimens with fragile curvature also tend to under-estimate laboratory field strengths.
6. Experimental protocols and selection criteria that do not test for curvature may yield inaccurate paleointensity results. It is not clear how to 'correct' for this behavior, so it is important to identify it using a curvature criterion.

Acknowledgments

Thanks are owed to Wyn Williams and Les Nagy for many useful discussions. This work was supported by NSF grants EAR1547263 and EAR1827263 to LT and by Australian Research Council grant DP190100874 to APR and LT. Data for this project are available at https://earthref.org/MagIC/16963/9b0be19b-e5bc-4cde-8aa4-a8116659542e for the purposes of review and will be made public upon acceptance of the manuscript.

References

Abokodair, A. (1977). The accuracy of the Thelliers technique for the determination of paleointensities of the Earth's magnetic field. *PhD Thesis, University of California Santa Cruz*.

Aitken, M., Alcock, P., Bussel, G., & Shaw, C. (1981). Archaeomagnetic determination of the past geomagnetic intensity using ancient ceramics: allowance for anisotropy. *Archaeometry*, *23*, 53-64.

Biggin, A. (2006). First-order symmetry of weak-field partial thermoremanence in multi-domain (MD) ferromagnetic grains: 2. Implications for Thellier-type palaeointensity determination. *Earth and Planet. Sci. Lett.*, *245*, 454-470. doi: 10.1016/j.epsl.2006.02.034

Biggin, A. (2010). Paleointensity database updated and upgraded. *EOS*, *91*, 15.

Cai, S., Tauxe, L., & Cromwell, G. (2017). Paleointensity from subaerial basltic glasses from the second Hawaii Scientific Drilling Project (HSDP2) core and implications for possible bias in data from lava flow interiors. *J .Geophys. Res.*, *122*, 8664-8674. doi: 10.1002/2017JB014683

Carvallo, C., Roberts, A., Leonhardt, R., Laj, C., Kissel, C., Perrin, M., & Camps, P. (2006). Increasing the efficiency of paleointensity analyses by selection of samples using first-order reversal curve diagrams. *J. Geophys. Res.*, *111*, B12103. doi: 10.1029/2005JB004126

Coe, R. S. (1967). The determination of paleo-intensities of the earth's magnetic field with emphasis on mechanisms which could cause non-ideal behavior in thellier's method. *J. Geomag. Geoelectr.*, *19*, 157–178.

Cromwell, G., Tauxe, L., Staudigel, H., Constable, C., Koppers, A., & Pedersen, R.-B. (2013). Evidence for long-term hemispheric asymmetry in the geomagneitc field: results from high northern latitudes. *Geochem. Geophys. Geosys.*, *14*. doi: 10.1002/ggge.20174

Cromwell, G., Tauxe, L., Staudigel, H., & Ron, H. (2015). Paleointensity estimates from historic and modern Hawaiian lava flows using basaltic volcanic glass as a primary source material. *Phys. Earth Planet. Int.*, *241*, 44-56. doi: 10.1016/j.pepi.2014.12.007

Cromwell, G., Trusdell, F., Tauxe, L., Staudigel, H., & Ron, H. (2018). Holocene paleointensity of the Island of Hawai'i from glassy volcanics. *Geochem. Geophys. Geosys.*, *19*, 3224-3245. doi: 10.1002/2017GC006927

Day, R., Fuller, M. D., & Schmidt, V. A. (1977). Hysteresis properties of titanomagnetites: grain size and composition dependence. *Phys. Earth Planet. Inter.*, *13*, 260–266.

Dunlop, D., & Özdemir, O. (2001). Beyond Néel's theories: thermal demagnetization of narrow-band partial thermoremanent magnetization. *Phys. Earth Planet. Int.*, *126*, 43-57.

Egli, R., Chen, A., & Winklhofer, M. (2010). Detection of noninteracting single domain particles using first-order reversal curve diagrams. *Geochem. Geophys. Geosys.*, *11*, Q01Z11. doi: 10.1029/2009GC002916

Fabian, K. (2001). A theoretical treatment of paleointensity determination experiments on rocks containing pseudo-single or multi domain magnetic particles. *Earth Planet. Sci. Lett.*, *188*, 45-48.

Fabian, K. (2003). Some additional parameters to estimate domain state from isothermal magnetization measurements. *Earth and Planetary Science Letters*, *213*(3-4), 337-345. doi: 10.1016/S0012-821X(03)00329-7

Fabian, K., Andreas, K., Williams, W., Heider, F., Leibl, T., & Huber, A. (1996). Three-dimensional micromagnetic calculations for magnetite using FFT. *Geophys. J. Int.*, *124*, 89-104.

Fabian, K., & Shcherbakov, V. (2018). Energy barriers in three-dimensional micromagnetic models and the physics of thermoviscous magnetization. *Geophys. J. Int.*, *215*, 314-324. doi: 10.1093/gji/ggy285

Halgedahl, S. L. (1993). Experiments to investigate the origin of anomalously elevated unblocking temperatures. *Jour. Geophys. Res.*, *98*, 22443–22460.

Harrison, R., Zhao, X., Hu, P., Sato, T., Heslop, D., Muxworthy, A., ... Roberts, A. (2019). Simulation of remanent, transient, and induced forc diagrams for interacting particles with uniaxial, cubic, and hexagonal anisotropy. *J. Geophys. Res*, *124*, 12404-12429. doi: 10.1029/2019jb018050

Koenigsberger, J. (1936). Die abhaengigkeit der natuerlichen remanenten magnetisierung bei eruptivgesteinen von deren alter und zusammensetzung. *Beitr. Angew. Geophys.*, *5*, 193-246.

Koenigsberger, J. (1938). Natural residual magnetism of eruptive rocks, Pt I, Pt II. *Terr. Magn. and Atmos. Electr.*, *43*, 119-127;299-320.

Krása, D., Heunemann, C., Leonhardt, R., & Petersen, N. (2003). Experimental procedure to detect multidomain remanence during Thellier-Thellier experiments. *Phys. Chem. Earth*, *28*, 681-687. doi: 10.1016/S1474-7065(03)00122-0

Lascu, I., Einsle, J., Ball, M., & Harrison, R. (2018). The vortex state in geologic materials: A micromagnetic perspective. *J Geophys Res-Solid Earth*, *123*, 7285-7304. doi: 10.1029/2018JB015909

Lawrence, K. P., Tauxe, L., Staudigel, H., Constable, C., Koppers, A., McIntosh, W. C., & Johnson, C. L. (2009). Paleomagnetic field properties near the southern hemisphere tangent cylinder. *Geochem. Geophys. Geosyst.*, *10*, Q01005. doi: doi:10.1029/2008GC002072

Muxworthy, A., Heslop, D., & Williams, W. (2004). Influence of magnetostatic interactions on first-order-reversal-curve (FORC) diagrams: A micromagnetic approach. *Geophys. J. Int.*, *158*, 888-897. doi: 10.1111/j.1365-246X.2004.02358.x

Nagy, L., Williams, W., Muxworthy, A., Fabian, K., Almeida, T., Conbhuiu, P., & Shcherbakov, V. (2017). Stability of equidimensional pseudo-single domain magnetite over billion year timescales. *Proc. Nat. Acad. Sci.*, *114*, 10356-10360. doi: 10.1073/pnas.1708344114

Néel, L. (1949). Théorie du trainage magnétique des ferromagneétiques en grains fines avec applications aux terres cuites. *Ann. Geophys.*, *5*, 99–136.

Néel, L. (1955). Some theoretical aspects of rock-magnetism. *Adv. Phys*, *4*, 191-243. doi: 10.1080/00018735500101204

Newell, A. (2005). A high-precision model of first-order reversal curve (FORC) functions for single-domain ferromagnets with uniaxial anisotropy. *Geochem. Geophys. Geosys.*, *6*, Q05010. doi: 10.1029/2004GC000877

Novosad, V., Guslienko, H., Shima, Y., Otani, K., Fukamichi, K., Kitakami, N., & Shimada, Y. (2001). Nucleation and annihilation of magnetic vortices in sub-micron permalloy dots. *IEEE Trans. Magn.*, *37*, 2088-2090. doi: 10.1109/20.951062

Paterson, G. (2011). A simple test for the presence of multidomain behavior during paleointensity experiments. *Journal of Geophysical Research*, *116*(B10). doi: 10.1029/2011JB008369

Paterson, G., Biggin, A., Hodgson, E., & Hill, M. (2015). Thellier-type paleointensity data from multidomain specimens. *Phys. Earth and Planet. Inter.*, *245*, 117-133. doi: 10.1016/j.pepi.2015.06.003

Paterson, G., Muxworthy, A., Yamamoto, Y., & Pan, Y. (2017). Bulk magnetic domain stability controls paleointensity fidelity. *Proceedings of the National Academy of Science*, *114*, 13120-13125. doi: 10.1073/pnas.1714047114

Pike, C., Roberts, A., & Verosub, K. (1999). Characterizing interactions in fine magnetic particle systems using first order reversal curves. *J. Appl. Phys.*, *85*, 6660-6667.

Pullaiah, G., Irving, E., Buchan, K., & Dunlop, D. (1975). Magnetization changes caused by burial and uplift. *Earth Planet. Sci. Lett.*, *28*, 133-143.

Roberts, A., Pike, C., & Verosub, K. (2000). First-order reversal curve diagrams: A

649 new tool for characterizing the magnetic properties of natural samples. *J. Geo-*
650 *phy. Res.*, *105*, 28461-28475. doi: 10.1029/2000JB900326
651 Santos, C., & Tauxe, L. (2019). Investigating the accuracy, precision, and cool-
652 ing rate dependence of laboratory acquired thermal remanences during pa-
653 leointensity experiments. *Geochem. Geophys. Geosys.*, *20*, 383-397. doi:
654 10.1029/2018GC007946
655 Sbarbori, E., Tauxe, L., Goguitchaichvili, A., Urrutia-Fucugauchi, J., & Bohrson, W.
656 (2009). Paleomagnetic behavior of volcanic rocks from Isla Socorro, Mexico.
657 *Earth, Planets and Space*, *61*, 191-204. doi: 10.1186/BF03352899
658 Schabes, M. E., & Bertram, H. N. (1988). Magnetization processes in ferromagnetic
659 cubes. *J. Appl. Phys.*, *64*, 1347–1357.
660 Selkin, P., Gee, J. S., & Tauxe, L. (2007). Nonlinear thermoremanence acquisition
661 and implications for paleointensity data. *Earth Planet. Sci. Lett.*, *256*, 81-89.
662 Shaar, R., & Tauxe, L. (2015). Instability of thermoremanence and the problem
663 of estimating the ancient geomagnetic field strength from non-single-domain
664 recorders. *Proceedings of the National Academy of Science*, *112*, 11187-11192.
665 doi: 10.1073/pnas.1507986112
666 Shashkanov, V., & Metallova, V. (1972). Violation of Thellier's law for partial ther-
667 moremanent magnetizations. *Izv. Earth Physics*, *3*, 80-86.
668 Smirnov, A., Kulakov, E., Foucher, M., & Bristol, K. (2017). Intrinsic paleointensity
669 bias and the long-term history of the geodynamo. *Sci. Adv.*, *3*. doi: 10.1126/
670 sciadv.1602306
671 Stacey, F. D., Lovering, J. F., & Parry, L. G. (1961). Thermomagnetic proper-
672 ties, natural magnetic moments, and magnetic anisotropies of some chondritic
673 meteorites. *J. Geophys. Res.*, *66*, 1523-1534.
674 Tanaka, H., & Kono, M. (1991). Preliminary results and reliability of palaeointensity
675 studies on historical and C^{14} dated Hawaiian lavas. *Journal of Geomagnetism*
676 *and Geoelectricity*, *43*, 375-388.
677 Tauxe, L., Banerjee, S. K., Butler, R., & van der Voo, R. (2010). *Essentials of Pale-*
678 *omagnetism*. Berkeley: University of California Press.
679 Tauxe, L., Bertram, H., & Seberino, C. (2002). Physical interpretation of hystere-
680 sis loops: Micromagnetic modelling of fine particle magnetite. *Geochem., Geo-*
681 *phys., Geosyst.*, *3*, doi:10.1029/2001GC000280.
682 Tauxe, L., Shaar, R., Jonestrask, L., Swanson-Hysell, N., Minnett, R., Kop-
683 pers, A. A. P., ... Fairchild, L. (2016). PmagPy: Software package for
684 paleomagnetic data analysis and a bridge to the Magnetics Information
685 Consortium (MagIC) database. *Geochem. Geophys. Geosys.*, *17*. doi:
686 10.1002/2016GC006307
687 Tauxe, L., & Staudigel, H. (2004). Strength of the geomagnetic field in the
688 Cretaceous Normal Superchron: New data from submarine basaltic glass
689 of the Troodos Ophiolite. *Geochem. Geophys. Geosyst.*, *5*(2), Q02H06,
690 doi:10.1029/2003GC000635.
691 Tauxe, L., & Yamazaki, T. (2015). Paleointensities. In M. Kono (Ed.), *Geomag-*
692 *netism* (2nd Edition ed., Vol. 5, p. 461-509). Elsevier.
693 Thellier, E. (1938). Sur l'aimantation des terres cuites et ses applications
694 géophysique. *Ann. Inst. Phys. Globe Univ. Paris*, *16*, 157-302.
695 Thellier, E., & Thellier, O. (1959). Sur l'intensité du champ magnétique terrestre
696 dans le passé historique et géologique. *Ann. Geophys.*, *15*, 285–378.
697 Williams, W., & Dunlop, D. J. (1989). Three-dimensional micromagnetic modelling
698 of ferromagnetic domain structure. *Nature*, *337*, 634–637.
699 Yu, Y., & Tauxe, L. (2005). On the use of magnetic transient hysteresis in paleo-
700 magnetism for granulometry. *Geochem. Geophys. Geosys.*, *6*, Q01H14. doi: 10
701 .1029/2004GC000839
702 Yu, Y., Tauxe, L., & Genevey, A. (2004). Toward an optimal geomagnetic field in-
703 tensity determination technique. *Geochemistry, Geophysics, Geosystems*, *5*(2),

Q02H07, doi:10.1029/2003GC000630.

Zhao, X., Heslop, D., & Roberts, A. (2015). A protocol for variable-resolution first-order reversal curve measurements. *Geochem. Geophys. Geosyst.*, *16*, 1364-1377. doi: 10.1002/2014GC005680

Zhao, X., Roberts, A., Heslop, D., Paterson, G., Li, Y., & Li, J. (2017). Magnetic domain state diagnosis using hysteresis reversal curves. *J. Geophys. Res.*, *122*, 4767-4789. doi: 10.1002/2016JB013683

Zijderveld, J. D. A. (1967). *A.C. demagnetization of rocks: Analysis of results.* Chapman and Hall.